JAAS
Journal of Analytical Atomic Spectrometry

Accepted Manuscript

This article can be cited before page numbers have been issued, to do this please use: T. Van Helden, S. Braeuer, T. Van Acker, O. Leroux, D. Van Der Straeten and F. Vanhaecke, *J. Anal. At. Spectrom.*, 2022, DOI: 10.1039/D2JA00131D.

ROYAL SOCIETY OF CHEMISTRY

rsc.li/jaas

View Article Online
DOI: 10.1039/D2JA00131D

TECHNICAL NOTE

High-speed mapping of Hg and Se in biological tissue via laser ablation – inductively coupled plasma – mass spectrometry

Tom Van Helden,[a] Simone Braeuer,[a,b] Thibaut Van Acker,[a] Olivier Leroux,[c] Dominique Van Der Straeten[c] and Frank Vanhaecke *[a]

Received 00th January 20xx,
Accepted 00th January 20xx

DOI: 10.1039/x0xx00000x

While elemental mapping via LA-ICP-MS – i.e. mapping the distribution of elements across the surface of a solid material – has shown a substantial evolution towards higher speed, sensitivity and spatial resolution, some elements show a significantly longer single pulse response (SPR) duration due to their specific physicochemical properties. This work focuses on Hg and Se as such elements in biological tissue and systematically investigates the effects of the instrumental setup, such as the type of ablation cell, mixing bulb and transfer line, on the shape and duration of the SPR profiles. By optimizing the instrumental setup, SPRs with a full peak width at 10% of the maximum peak height (FW0.1M) at a laser spot size of 20 µm diameter of 50 ± 2 and 61 ± 4 ms were obtained for $^{202}Hg^+$ and $^{77}Se^+$, respectively. This constitutes a >5-fold improvement in SPR duration compared to a standard setup, but these SPR durations are still considerable longer than those obtained for, *e.g.*, $^{65}Cu^+$ (7 ± 1 ms). When selecting the instrument settings and data acquisition conditions for elemental mapping of Hg and/or Se based on the SPR profiles obtained for, *e.g.*, $^{65}Cu^+$, the pixel acquisition rate attainable was overestimated for $^{202}Hg^+$ and $^{77}Se^+$ and significant aerosol carryover or pixel crosstalk occurs, thus leading to smearing effects in the elemental maps. With the optimum setup and adequate selection of all settings, multi-elemental mapping of Hg and Se was performed for a mushroom tissue section, demonstrating a significant improvement in pixel acquisition rate (up to 20 pixels s^{-1}).

Introduction

Especially during the last decade, developments in the field of laser ablation-inductively coupled plasma-mass spectrometry (LA-ICP-MS) have led to substantial progress in the context of elemental mapping. So-called ultra-fast ablation cells and low-dispersion aerosol transport systems transfer the aerosol generated upon laser-sample interaction in a highly efficient and rapid manner to the ICP.[1-6] Use of a high-velocity laminar gas flow transporting the aerosol cloud from the ablation cell into the ICP ion source strongly limits diffusion, as a result of which the sample material, removed by each laser pulse, is reaching the ICP within a shorter time window, thus resulting in transient signals characterized by a shorter single pulse response (SPR) duration. A short SPR duration allows a considerable higher laser repetition rate to be applied, and thus greatly improves the speed of analysis. In addition, the compression of sample material in a shorter spatial, and thus also temporal, window also brings about a substantial enhancement in signal-to-noise (S/N) ratios, thus permitting the use of laser beams with a smaller diameter. As a result, elemental mapping can be carried out at higher spatial resolution (down to sub-µm) and at higher speed (up to 1 kHz pixel acquisition rate) than ever before.[3,4] For fully exploiting the improved capabilities of such setup, especially when using a sequential scanning-type ICP-mass spectrometer for multi-element mapping, an adequate selection of the instrument settings and data acquisition parameters is required to avoid interference patterns due to aliasing effects.[7] A profound understanding of the interplay between the SPR and data acquisition parameters has greatly improved the overall image quality. Combined with successful efforts in the development of calibration approaches, these advances have resulted in LA-ICP-MS being an increasingly valuable technique in many application areas.[8-12]

In pneumatic nebulization-ICP-MS (PN-ICP-MS), some elements, *e.g.*, Hg, are well known (or rather infamous) for their long washout due to so-called "memory effects".**[13,14]** In the case of Hg, this is attributed to the stickiness of some of its compounds towards the tubing material and is counteracted by the addition of Cl^- ions, Au^{3+} ions, NH_3 or a strong oxidizer to the sample solution.[13,15] Previous publications describing the use of LA-ICP-MS for the determination of Hg already reported on partial sorption of Hg vapour onto the inner surface of the aerosol transfer tubing and ablation cell followed by slow desorption, resulting in a considerably longer SPR duration than for the majority of the other elements.[16] In some cases, this observation was ignored and no specific action was taken to cope with these longer SPR durations.[17-19] In other cases, strategies such as lowering of the overall scanning speed[20-22] or introducing a waiting time between scans to allow the signal to return to background levels were introduced.[16, 23-25] Also Se,

---

[a] Atomic & Mass Spectrometry – A&MS research unit, Department of Chemistry, Ghent University, Campus Sterre, Krijgslaan 281 - S12, 9000 Ghent, Belgium

[b] Institute of Chemistry, Analytical Chemistry, University of Graz, Universitaetsplatz 1, 8010 Graz, Austria

[c] Laboratory of Functional Plant Biology, Department of Biology, Ghent University, K.L. Ledeganckstraat 35, 9000 Ghent, Belgium

† Footnotes relating to the title and/or authors should appear here.

Electronic Supplementary Information (ESI) available: [details of any supplementary information available should be included here]. See DOI: 10.1039/x0xx00000x another element of considerable importance in a bio-context, was found to show an ablation and/or transport behaviour that leads to a longer SPR duration than the majority of the other elements. The target elements in this work – Hg and Se – were not only selected on the basis of their physicochemical properties and the corresponding longer SPR duration, but also because of their biological and environmental relevance. Hg (especially in its methylated form $MeHg^+$) is known for its toxicity. Several studies have demonstrated a relationship between Hg and Se and a possible Se-Hg antagonism (*i.e.* detoxification of Hg by Se) is addressed in many papers.[18,26-29] To obtain high-quality Hg and/or Se maps with sequential scanning-type ICP-mass spectrometers, all instrument settings and data acquisition conditions have to be carefully selected and/or synchronized to accommodate for these longer SPR durations, which has several important consequences. Obviously, a long SPR duration will reduce the pixel acquisition rate and thus increase measurement time and reduce sample throughput, but it will also negatively affect the S/N ratio, which in turn may require an increase in beam diameter as compensation, deteriorating the spatial resolution of the elemental map.[2] In addition, multi-element analysis can also become more challenging due to the relative differences in SPR durations between different elements.

In this work, it was demonstrated how an optimized instrument configuration reduces the SPR duration, allowing Hg and Se mapping at the highest possible pixel acquisition rate, while avoiding aliasing effects.[30] The SPR profiles and the corresponding effects on the image quality were systematically assessed for Hg, Se and Cu (for comparison purposes) using several setups. Experimental characteristics, such as the type of ablation cell, mixing bulb and the inner diameter (ID) and length of the aerosol transport tubing were studied in order to shed light on the mechanisms influencing the SPR duration and to provide some insight as to how to improve experimental parameters with some easy and low-cost measures. To demonstrate the capabilities of the optimized setup, multi-elemental mapping was performed for a tissue section of *Boletus edulis*, which is known for accumulating significant amounts of Hg and Se.[31] To the best of the authors' knowledge, this is the first publication describing LA-ICP-MS mapping of Hg and Se with an LA-unit equipped with a low-dispersion aerosol transport system.

Experimental

Preparation of gelatin droplet standards

A 10% (m/m) solution of gelatin (VWR International, Leuven, Belgium) was prepared in ultra-pure water (resistivity ≥ 18.2 MΩ cm at 25 °C) and spiked with varying amounts of Hg, Se and Cu originating from commercially available 1,000 mg L^{-1} stock solutions (Inorganic Ventures, Christiansburg, VA, USA) to achieve gelatin droplets containing 5, 25 and 5 µg g^{-1} of Hg, Se and Cu, respectively. The solutions were heated at 55 °C for 1 h prior to vortex mixing to ensure good homogeneity. After homogenization, small droplets of approximately 10 µL were deposited on a Superfrost™ soda-lime-silica glass microscope slide (Thermo Fisher Scientific, Waltham, MA, USA) and dried at room temperature.

Preparation of mushroom tissue sections

View Article Online
DOI: 10.1039/D2JA00131D

Blocks not exceeding 1x1x1 cm^3 in volume were excised from the stipe of a frozen *Boletus edulis* fruit body. Tissue-Plus O.C.T. medium (Fisher Scientific, Waltham, MA, USA) was used to firmly fix the tissue blocks onto the sample holder by freezing at -45 °C in a cryostat (Thermo Shandon FSE, Waltham, MA, USA). After trimming of the frozen tissue blocks, 10 µm sections were cut and collected on cryo-compatible adhesive tape segments (Cryofilm 2C, Section-Lab, Hiroshima, Japan). These were placed onto polylysine-coated slides with the sections facing upwards and stored in a slide box at -20 °C until analysis.

Overview of instrumental setups

Two different nanosecond 193 nm ArF*excimer-based LA-units were used with a variety of aerosol transport systems to evaluate their effects on the transport of LA-generated aerosols and the duration of the SPR durations for Hg and Se. The first LA-unit is an Analyte G2 equipped with a two-volume HelEx-II cup-type ablation cell (Teledyne Photon Machines, Bozeman, MT, USA). The second LA-unit is an Iridia equipped with a Cobalt ablation chamber and optimized cup-type ablation cell (Teledyne Photon Machines, Bozeman, MT, USA).[3] Both units were coupled to an Agilent 7900 quadrupole-based ICP-MS instrument (Agilent Technologies, Tokyo, Japan). Two mixing bulbs were evaluated, *i.e.* the Aerosol Rapid Introduction System (ARIS, originally developed at A&MS-UGent and meanwhile commercially available from Teledyne Photon Machines, Bozeman, MT, USA)[4] and a glass mixing bulb (Glass Expansion, Weilburg, Germany), directly connected to the ICP torch inlet. The LA cells were connected to the mixing bulbs by using PEEK tubing of various length (1.5, 0.9 and 0.5 m) and internal diameters (1.00 and 0.75 mm ID). For every experiment, the settings were tuned for high sensitivity across the elemental mass range, low oxide ratios (evaluated via the $^{238}U^{16}O^+/^{238}U^+$ ratio) and low elemental fractionation (evaluated via the $^{238}U^+/^{232}Th^+$ ratio ≈ 1) while ablating NIST SRM 610 certified reference material (Trace Elements in Glass, Gaithersburg, USA). An overview of all setups used is provided in Table 1.

Table 1 (double-column)

Characterization of the SPR durations for Hg, Se and Cu

To evaluate the effects of the different components of an aerosol transport system, *e.g.* ablation cell, tubing and mixing bulb, on the aerosol transport and the resulting peak profiles, the SPR durations were determined for $^{202}Hg^+$, $^{77}Se^+$ and $^{65}Cu^+$ upon ablation of a gelatin droplet standard with all of the instrumental setups listed in Table 1. For every setup and nuclide, 100 laser pulses were fired on the surface of a gelatin droplet standard according to a line scan of 400 µm length using a low laser repetition rate of 1 Hz to achieve fully resolved peak profiles in all cases, an energy density of 1.5 J cm^{-2}, a dosage of 5 shots $position^{-1}$ and a circular laser beam of 20 µm diameter. All setup characteristics, instrument settings and data acquisition conditions can be found in Table S1.† Since differences in tubing diameter and length affect the internal pressure inside the ablation chamber, the He carrier gas flow rate was always adjusted to maintain a constant pressure between setups to only evaluate the effect of the parameters of interest and to allow direct comparison between different setups.

Effect of the pixel acquisition rate on the image quality

A mapping experiment was designed to demonstrate the detrimental effects on the Hg image quality when selecting the LA-ICP-MS instrument settings and data acquisition conditions based on the narrow SPR profiles obtained for a nuclide not affected by significant memory effects, *e.g.*, $^{65}Cu^+$. A range of pixel acquisition rates (4-50 pixels s^{-1}) was evaluated by varying the laser repetition rate (20-250 Hz), lateral scan speed (80-1,000 µm s^{-1}) and $^{202}Hg^+$ integration time (4-250 ms), but keeping the dosage, *i.e.* the number of laser shots fired per pixel position (which equals the ratio of the laser repetition rate over the pixel acquisition rate), constant at 5 shots per position (Table 2), in order to avoid aliasing and only evaluate the effect of aerosol carryover or pixel crosstalk and thus, smearing on the image quality.[7] Five adjacent regions of the same mushroom tissue section were analyzed at increasing pixel acquisition rates.

Table 2 (single-column)

Multi-elemental LA-ICP-MS mapping of fungal tissue

Multi-elemental maps of a mushroom tissue section were generated via LA-ICP-MS mapping using the fastest setup possible. In addition to the challenging elements Hg and Se, an element with a narrow SPR profile was analyzed to serve as comparison. Ag was selected due to the relatively high natural concentrations in mushrooms.[31] Multi-element analyses were performed in two pairs: a slow-fast combination (Hg and Ag) and a slow-slow combination (Hg and Se). Prior to analysis, SPR durations of these elements were determined in order to select (non-)optimized settings (Table S2†).

Data processing

All data obtained were processed using HDIP software (version 1.3.3.1091). ICP-MS data in the form of a .csv file and laser log files were imported and synchronized prior to signal background correction. For mapping experiments, the 1D .csv file was split into 2D elemental maps based on the laser time trace. The peak detection tool of HDIP was used to detect all individual peaks and construct the average SPR profiles. Graphs were constructed via OriginPro (version 9.0) and Matlab (version 9.11).

Results and discussion

Characterization of the SPR durations for Hg, Se and Cu

The average durations of the SPRs for $^{202}Hg^+$, $^{77}Se^+$ and $^{65}Cu^+$ obtained for each instrumental setup were calculated based on the FW0.1M criterion, *i.e.* full peak width at 10% of the maximum peak height, and are displayed in Figure 1a with their corresponding standard deviation as error bars (n = 100 peaks). The numerical values of Figure 1a are listed in Supplementary Information Table S3†. Setups A and B differ from one another in the type of mixing bulb used. While the use of the ARIS improves the SPR duration for all nuclides, the effect is most pronounced for $^{65}Cu^+$ (105 ± 2 vs. 28 ± 5 ms). For the setups C – E, the He gas flow rate was increased from 0.360 to 0.430 and 0.500 L min^{-1}, respectively, and it can be seen that SPR duration is inversely related to the He gas flow rate for all nuclides and that in this range of He gas flow rates, the relative reduction is equal for all nuclides. By comparing the results for setups F and G, both with the Cobalt ablation chamber, it can be seen that a reduction in tubing length with a factor of 1.8 (from 90 to 50 cm) results in a reduction to the same extent for the $^{77}Se^+$ SPR duration (109 ± 4 vs. 61 ± 4 ms, factor 1.8), but only has a negligible effect on the SPR durations for $^{65}Cu^+$ and $^{202}Hg^+$. Overall, setup G was found to be the fastest for all nuclides with average SPR durations of 7 ± 1, 61 ± 4 and 50 ± 2 ms for $^{65}Cu^+$, $^{77}Se^+$ and $^{202}Hg^+$, respectively. In Figure 1b, the average SPR profiles for all three nuclides are plotted for setup G and the signal intensities were normalized to the corresponding peak maxima to enable direct comparison of the peak profiles.

Figure 1 (single-column)

Between setups B and C, both the tubing length (1.5 to 0.9 m) and its internal diameter (1.00 to 0.75 mm) were changed and the He gas flow rate was reduced significantly (from 0.700 to 0.360 L min^{-1}) to maintain the same internal pressure in the HelEx-II ablation chamber. Taking into account that the $^{77}Se^+$ SPR duration is reduced to the same relative extent as the reduction in tubing length, while hypothetically assuming that a decrease in tubing diameter would lead to a quadratic increase of the SPR duration, one would expect the $^{77}Se^+$ SPR duration to increase from 162 to 173 ms , which closely matches the experimentally derived value of 171 ± 20 ms. On the contrary, for $^{65}Cu^+$ and $^{202}Hg^+$, this was not the case and a large increase in SPR duration was observed for $^{202}Hg^+$ (166 ± 10 vs. 358 ± 35 ms). Since it is known that Hg in the gas phase partially adsorbs onto the inner walls of the aerosol transport tubing and slowly desorbs over time, a decrease in tubing diameter and the corresponding increase in surface-to-volume ratio could promote adsorption, leading to a significantly longer SPR duration. Experiments E and F were performed with a different LA unit, equipped with another type of ablation cell, while the aerosol transfer tubing, mixing bulb and internal pressure were kept the same. Between these setups, a decrease in SPR duration was observed for all three elements, but the effect was much more pronounced for $^{65}Cu^+$ (33 ± 6 vs. 8 ± 1 ms) and $^{202}Hg^+$ (265 ± 20 vs. 56 ± 2 ms) than for $^{77}Se^+$ (128 ± 12 vs. 109 ± 4). To ensure that the observation for $^{77}Se^+$ was not due to spectral interference, the experiment was repeated for ^{76}Se, ^{78}Se and ^{82}Se with the same outcome

A more in-depth evaluation was performed in an attempt to understand the behaviour displayed in the Se peak profiles and in Figure 1c, the $^{77}Se^+$ SPR profiles are provided for setups F and G (15 ms integration time), as well as the $^{77}Se^+$ SPR profile for setup G monitored with a shorter integration time of 10 ms. For setup F, the $^{77}Se^+$ SPR profile shows two local peak maxima

View Article Online
DOI: 10.1039/D2JA00131D

suggesting the presence of two distinct phases in the LA-generated aerosol. Since the profile and duration of the broader second peak closely matches the peak profile for $^{202}Hg^+$, which is assumed to be transported predominantly in the gaseous phase, it is hypothesized that the second peak corresponds to Se transported in the gaseous phase. The first peak more closely resembles the profile of $^{65}Cu^+$, suggesting that this corresponds to Se being transported in the particulate phase.[32] For setup G, initially the two local peak maxima were not observed but when monitoring at a shorter integration time of 10 ms, both peak maxima were revealed again. This difference could be attributed to a smaller difference in arrival time in the ICP between the particulate and gaseous phase of Se due to the shorter tubing length for setup G compared to F.

All components and parameters that were investigated, affect the SPR duration of all three elements, but to a different degree. For Cu, the largest relative improvement was observed upon changing the mixing bulb and using a low-dispersion ablation cell. For Se, the largest relative improvement was realized by reducing the tubing length, and for Hg, changing the type of ablation cell had the largest effect. For multi-elemental mapping of Cu, Se and Hg, this would indicate that the optimal setup would be comprised of a low-dispersion ablation cell with high internal pressure connected to the ICP torch inlet through short tubing and the ARIS mixing bulb.

Effect of the pixel acquisition rate on the image quality

Figure 2 shows the importance of carefully selecting the instrument settings and data acquisition conditions (Table 2) in function of the SPR duration, which was approximately 20 and 250 ms for $^{65}Cu^+$ and $^{202}Hg^+$, respectively (non-optimized setup). Different regions of a mushroom tissue section were analyzed under increasingly fast conditions with a laser spot size of 20 µm diameter. The pixel acquisition rate was increased stepwise from 4 to 50 pixels s^{-1} and $^{202}Hg^+$ was monitored with stepwise decreasing integration times (250 to 20 ms). It can be seen that as the measurement speed increases, the $^{202}Hg^+$ maps obtained exhibit more and more smearing, decreasing the overall quality. Based on the $^{202}Hg^+$ SPR profiles, it was estimated that the pixel crosstalk increased from <5 % to >90%.

Figure 2 (double-column)

Multi-elemental LA-ICP-MS mapping of fungal tissue

To demonstrate the improved capabilities of the optimized setup G, multi-elemental maps of a mushroom fruit body thin section were generated (Figure 3) for combinations of (i) two "slow" elements (Hg and Se) and (ii) a "slow" and "fast" element (Hg and Ag). All signal intensities of the different nuclides were normalized to enable direct comparison of the maps. The $^{202}Hg^+$ and $^{77}Se^+$ map at the top of Figure 3 were generated at a pixel acquisition rate of 100 and 20 pixels s^{-1}, which are non-matched and matched conditions to the SPR profiles, respectively. At a pixel acquisition rate of 100 pixels s^{-1}, the pixel crosstalk is estimated at >50% for both nuclides and significant smearing effects can be observed in the maps, while at 20 pixel s^{-1}, no significant smearing effects can be seen.

Figure 3 (double-column)

Compromises have to be made when monitoring multiple nuclides with a larger difference in SPR duration, *e.g.*, $^{202}Hg^+$ and $^{107}Ag^+$. The implementation of an ultra-fast low-dispersion ablation cell and aerosol transport system can significantly improve the SPR durations of Hg and Se, even though they remain still considerably longer than the SPR durations of most other elements. Image quality will not decrease substantially for "fast" elements when an acquisition rate is used that is matched to "slow" elements as can be seen in the $^{202}Hg^+$ and $^{107}Ag^+$ maps acquired at 20 pixels s^{-1}, displayed at the bottom of Figure 3. When the instrument settings and data acquisition conditions are unmatched to the "slow" element, significant smearing effects can be observed, as shown in the $^{202}Hg^+$ map acquired at 100 pixels s^{-1}. In contrast to the $^{202}Hg^+$ map in Figure 2, generated at 4 pixels s^{-1} and acquired using a non-optimized setup, high-quality multi-elemental maps were generated at a pixel acquisition rate of 20 pixels s^{-1} (5-fold faster). In a similar approach, the proposed method can be expanded to mapping experiments addressing more than two elements. With (sequential) ICP-Q-MS instrumentation, the total scan cycle time (sum of individual dwell and settling times) should be equal to the SPR duration (in this case 50 ms), and should be distributed over multiple target elements, which will permit monitoring of 4 – 5 elements, depending on the settling time added by the system. If analysis of even more elements is desired, the use of a "simultaneous" type of ICP-MS instrumentation, such as ICP-TOF-MS is advisable.

Conclusions

When aiming at high-quality LA-ICP-MS mapping of elements characterized by a longer SPR duration, two important aspects have to be taken into account. First, the analysis speed can be greatly improved by optimizing the experimental setup aiming at narrower peak profiles. Successful alterations in decreasing the single pulse response duration depend on the physicochemical properties of the element of interest and include changing tubing length or inner diameter or, if available, use of a low-dispersion ablation cell. We have postulated that some elements are transported in the particulate phase (Cu), other in the gas (Hg) phase, and some distributed over both phases (Se), and that the SPR duration is significantly shorter for elements transported in the particulate phase. For a full understanding, future research should focus on the fundamental causes of this different behaviour and evaluate to what extent changing measurement parameters, such as laser fluence or pulse length influence the SPR duration. When an optimized SPR has been achieved, measurement conditions have to be carefully chosen in function of the "slowest" element to ensure elemental maps of the highest resolution and quality by avoiding smearing and aliasing effects. This can open the way

View Article Online
DOI: 10.1039/D2JA00131D

towards new application types for which high-resolution mapping is crucial. With the same approach, it is possible to perform multi-elemental mapping, even when there is a significant difference in SPR duration between the elements of interest, thus allowing fast mapping of new combinations of elements. Especially in the context of the Se – Hg antagonism, the ability to obtain information on co-localization of either or both Se/Hg with other elements opens up new possibilities for future research. Under optimized conditions, the SPR durations of $^{202}Hg^+$ and $^{77}Se^+$ could be reduced to 50 ± 2 and 61 ± 4 ms (FW0.1M), respectively, enabling mapping of these two elements at a pixel acquisition rate of 20 pixels s^{-1} with limited pixel crosstalk.

Conflicts of interest

Tom Van Helden, Simone Braeuer, Thibaut Van Acker and Frank Vanhaecke work in the A&MS-UGent research unit that has licensed intellectual property to Teledyne CETAC Technologies. The ultra-fast tube-type ablation cell that the Cobalt cell is based on, the ARIS and the HDIP software were originally developed at A&MS-UGent and are meanwhile commercially available through Teledyne CETAC Technologies. The other authors have no conflict of interest.

Acknowledgements

Simone Braeuer acknowledges the Austrian Science Fund FWF (Schroedinger project number J 4400-N). Thibaut Van Acker acknowledges Ghent University's Bijzonder Onderzoeksfonds (BOF-UGent grant number PDO2020003501). The work of Olivier Leroux was supported by Ghent University (GOA01G00409 granted by Bijzonder Onderzoeksfonds-UGent to Dominique Van Der Straeten). Frank Vanhaecke acknowledges the Flemish Research Foundation (FWO-Vlaanderen) for financial support under the form of research project G017217N.

Notes and references

1 S. J. Van Malderen, J. T. van Elteren and F. Vanhaecke, *J. Anal. At. Spectrom.*, 2015, **30**, 119-125.
2 S. J. Van Malderen, A. J. Managh, B. L. Sharp and F. Vanhaecke, *J. Anal. At. Spectrom.*, 2016, **31**, 423-439.
3 S. J. Van Malderen, T. Van Acker and F. Vanhaecke, *Anal. Chem.*, 2020, **92**, 5756-5764.
4 T. Van Acker, S. J. Van Malderen, T. Van Helden, C. Stremtan, M. Šala, J. T. van Elteren and F. Vanhaecke, *J. Anal. At. Spectrom.*, 2021, **36**, 1201-1209.
5 A. Gundlach-Graham and D. Günther, *Anal. Bioanal. Chem.*, 2016, **408**, 2687-2695.
6 S. Theiner, S. Van Malderen, T. Van Acker, A. Legin, B. Keppler, F. Vanhaecke and G. Koellensperger, *Anal. Chem.*, 2017, **89**, 12641-12645.
7 J. T. van Elteren, V. S. Šelih, M. Šala, S. J. Van Malderen and F. Vanhaecke, *Anal. Chem.*, 2018, **90**, 2896-2901.
8 M. Šala, V. S. Šelih and J. T. van Elteren, *Analyst*, 2017, **142**, 3356-3359.
9 O. Hachmöller, M. Aichler, K. Schwamborn, L. Lutz, M. Werner, M. Sperling, A. Walch and U. Karst, *J. Trace Elem. Med. Biol.*, 2016, **35**, 97-102.
10 V. L. Dressler, E. I. Müller and D. Pozebon, in *Metallomics*, Springer, 2018, pp. 139-181.
11 B. Crone, L. Schlatt, R. A. Nadar, N. W. M. van Dijk, N. Margiotta, M. Sperling, S. Leeuwenburgh and U. Karst, *J. Trace Elem. Med. Biol.*, 2019, **54**, 98-102.
12 J.-C. Müller, M. Horstmann, L. Traeger, A. U. Steinbicker, M. Sperling and U. Karst, *J. Trace Elem. Med. Biol.*, 2019, **52**, 166-175.
13 Y. Li, C. Chen, B. Li, J. Sun, J. Wang, Y. Gao, Y. Zhao and Z. Chai, *J. Anal. At. Spectrom.*, 2006, **21**, 94-96.
14 P. R. Craddock, O. J. Rouxel, L. A. Ball and W. Bach, *Chem. Geol.*, 2008, **253**, 102-113.
15 J. Allibone, E. Fatemian and P. J. Walker, *J. Anal. At. Spectrom.*, 1999, **14**, 235-239.
16 M. Debeljak, J. T. van Elteren, K. Vogel-Mikus, *Anal. Chim. Acta*, 2013, **787**, 155-162.
17 M. Monperrus, C. Pécheyran and V. Bolliet, *Appl. Sci.*, 2020, **10**, 2463.
18 J. Liu, J. Cui, X. Wei, W. Li, C. Liu, X. Li, M. Chen, Y. Fan and J. Wang, *Anal. Chim. Acta*, 2021, 338941.
19 M. Iwase, Y.-k. Tanaka, N. Suzuki and Y. Ogra, *Toxicol. Sci.*, 2021, **46**, 193-198.
20 A. Kavčič, K. Mikuš, M. Debeljak, J. T. van Elteren, I. Arčon, A. Kodre, P. Kump, A. G. Karydas, A. Migliori and M. Czyzycki, *Ecotoxicol. Environ. Saf.*, 2019, **184**, 109623.
21 M. Debeljak, J. T. van Elteren, A. Špruk, A. Izmer, F. Vanhaecke and K. Vogel-Mikuš, *Chemosphere*, 2018, **212**, 1076-1084.
22 R. Pamphlett, P. A. Doble and D. P. Bishop, *Toxics*, 2021, **9**, 67.
23 M. Legrand, R. Lam, M. Jensen-Fontaine, E. D. Salin and H. M. Chan, *J. Anal. At. Spectrom.*, 2004, **19**, 1287-1288.
24 T. Bechshoft, Y. Luo, A. M. Bohart, A. E. Derocher, E. S. Richardson, N. J. Lunn and D. G. Pearson, *Ecol. Indic.*, 2020, **119**, 106822.
25 M. Noël, J. R. Christensen, J. Spence and C. T. Robbins, *Sci. Total Environ.*, 2015, **529**, 1-9.
26 Z. Gajdosechova, M. M. Lawan, D. S. Urgast, A. Raab, K. G. Scheckel, E. Lombi, P. M. Kopittke, K. Loeschner, E. H. Larsen and G. Woods, *Sci. Rep.*, 2016, **6**, 1-11.
27 M. A. Subirana, L. Paton, J. Hall, A. Brownlow, E. M. Krupp, J. r. Feldmann and D. Schaumlöffel, *Anal. Chem.*, 2021.
28 E. Bolea-Fernandez, A. Rua-Ibarz, E. M. Krupp, J. Feldmann and F. Vanhaecke, *Sci. Rep.*, 2019, **9**, 1-10.
29 Z. Gajdosechova, Z. Mester, J. Feldmann and E. M. Krupp, *TrAC - Trends Anal. Chem.*, 2018, **104**, 95-109.
30 J. T. van Elteren, V. S. Šelih and M. Šala, *J. Anal. At. Spectrom.*, 2019, **34**, 1919-1931.
31 J. Falandysz, T. Kunito, R. Kubota, L. Bielawski, A. Frankowska, J. J. Falandysz and S. Tanabe, *J. Environ. Sci. Health - Part A*, 2008, **43**, 1692-1699.
32 A. Limbeck, P. Galler, M. Bonta, G. Bauer, W. Nischkauer and F. Vanhaecke, *Anal. Bioanal. Chem.*, 2015, **407**, 6593-6617.

View Article Online
DOI: 10.1039/D2JA00131D

Tables

Table 1. List of different instrumental setups with specifications for ablation chamber, tubing length and inner diameter (ID), mixing bulb, He gas flow rate and ablation chamber pressure.

Setup	A	B	C	D	E	F	G
LA unit	Analyte G2	Analyte G2	Analyte G2	Analyte G2	Analyte G2	Iridia	Iridia
Ablation chamber	HelEx-II	HelEx-II	HelEx-II	HelEx-II	HelEx-II	Cobalt	Cobalt
Tubing length (cm)	150	150	90	90	90	90	50
Tubing ID (mm)	1	1	0.75	0.75	0.75	0.75	0.75
Mixing bulb	Glass mixing bulb (GE)	ARIS	ARIS	ARIS	ARIS	ARIS	ARIS
He gas flow rate (mL min^{-1})	700	700	360	430	500	360	500
Pressure ablation chamber (bar)	1.14	1.14	1.13	1.16	1.18	1.18	1.18

Table 2. Operating conditions for LA-ICP-MS mapping of Hg to evaluate the image quality in relation to the pixel acquisition rate. Parameters indicated by an * were changed to maintain synchronization and avoid aliasing effects.

Teledyne CETAC Technologies Analyte G2 LA system	
Repetition rate (Hz)*	20, 50, 125, 200 and 250
Energy density (J cm^{-2})	1.50
He carrier gas flow rate (L min^{-1})	0.500
Beam waist diameter (µm)	20
Mask shape	○
Dosage	5
Scan speed (µm s^{-1})	80, 200, 500, 800 and 1000
Agilent 7900 ICP-MS instrument	
RF power (W)	1500
Sampling depth (mm)	5.1
Plasma gas flow rate (L min^{-1})	15.0
Nebulizer gas flow rate (L min^{-1})	1.00
Nuclide monitored	^{202}Hg^{+}
Integration time (ms)*	250, 100, 40, 25 and 20
Pixel Acquisition Rate (Hz) *	4, 10, 25, 40 and 50

Figures

View Article Online
DOI: 10.1039/D2JA00131D

Figure 1. (a) Average SPR durations for $^{202}Hg^+$ (dark blue), $^{77}Se^+$ (blue) and $^{65}Cu^+$ (light blue), defined as FW0.1M, and corresponding standard deviations for each instrumental setup (n=100 shots). (b) Average SPR profiles for $^{202}Hg^+$ (dark blue), $^{77}Se^+$ (blue) and $^{65}Cu^+$ (light blue) for setup G normalized to the peak maxima. (c) Average SPR profiles for $^{77}Se^+$ obtained using an integration time time of 15 ms for setups F (blue) and G (green) normalized to the peak maxima. The orange line represents the average SPR profile for $^{77}Se^+$ using a shorter integration time of 10 ms.

Figure 2. Elemental maps of $^{202}Hg^+$ at various pixel acquisition rates, from top to bottom: 4, 10, 25, 40 and 50 pixels s^{-1}, by varying the integration time and laser repetition rate but keeping the laser energy density (1.5 J cm^{-2}), spot size (20 µm diameter) and dosage (5 shots per position) constant. The white scale bar corresponds to 200 µm.

Figure 3. Multi-elemental maps of $^{202}Hg^+$ and $^{77}Se^+$ (top) and $^{202}Hg^+$ and $^{107}Ag^+$ (bottom) for a mushroom fruit body tissue. These two mapping experiments were performed with the same, optimized setup but using different parameters – *i.e* a pixel acquisition rate of 100 vs. 20 Hz, which are non-matched and matched to the SPR duration for $^{202}Hg^+$, respectively. The laser beam waist diameter was 10 µm, the fluence 1.5 J/cm² and dosage 5, and a laser repetition rate of 500 Hz or 100 Hz was used for the non-matched and matched experiments, respectively. The color bars (top: $^{107}Ag^+$ or $^{77}Se^+$, bottom: $^{202}Hg^+$) were normalized to 100% for all nuclides and maps. The white scale bars correspond to 200 µm.

View Article Online
DOI: 10.1039/D2JA00131D

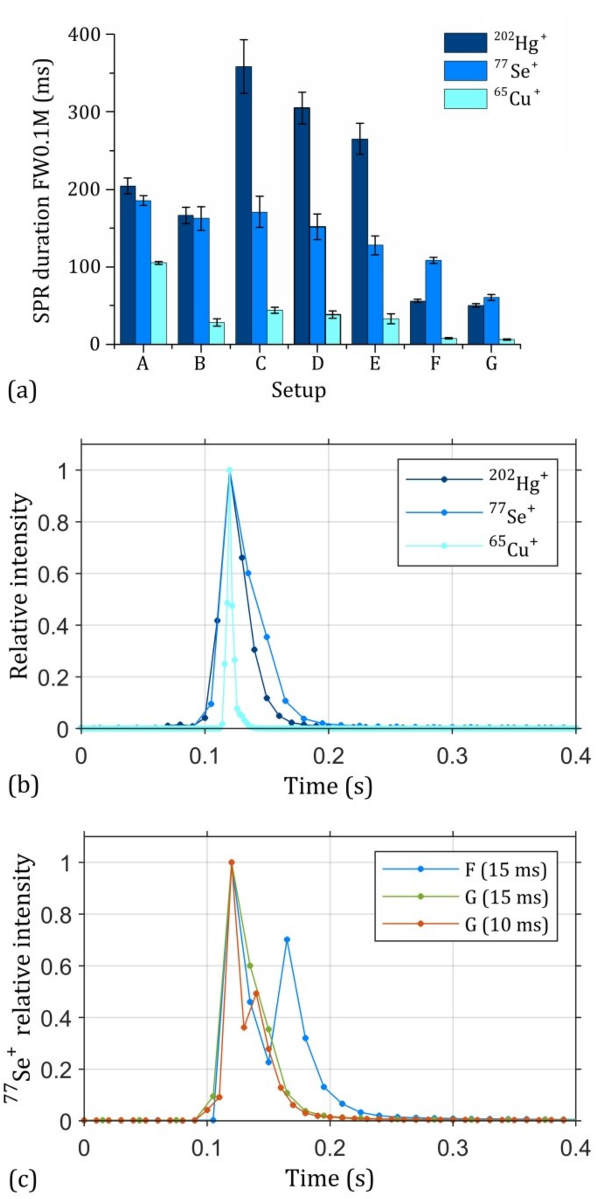

Figure 1

82x166mm (600 x 600 DPI)

View Article Online
DOI: 10.1039/D2JA00131D

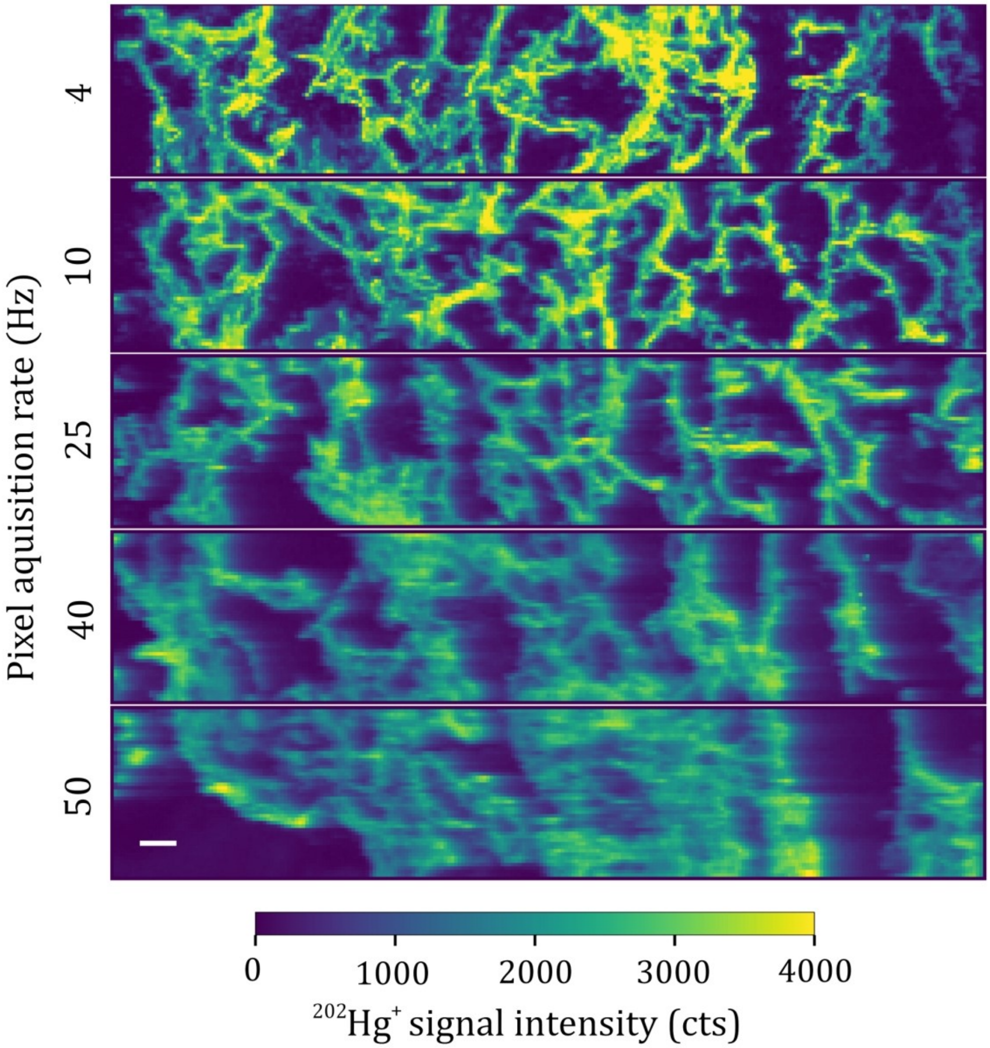

Figure 2

82x89mm (600 x 600 DPI)

View Article Online
DOI: 10.1039/D2JA00131D

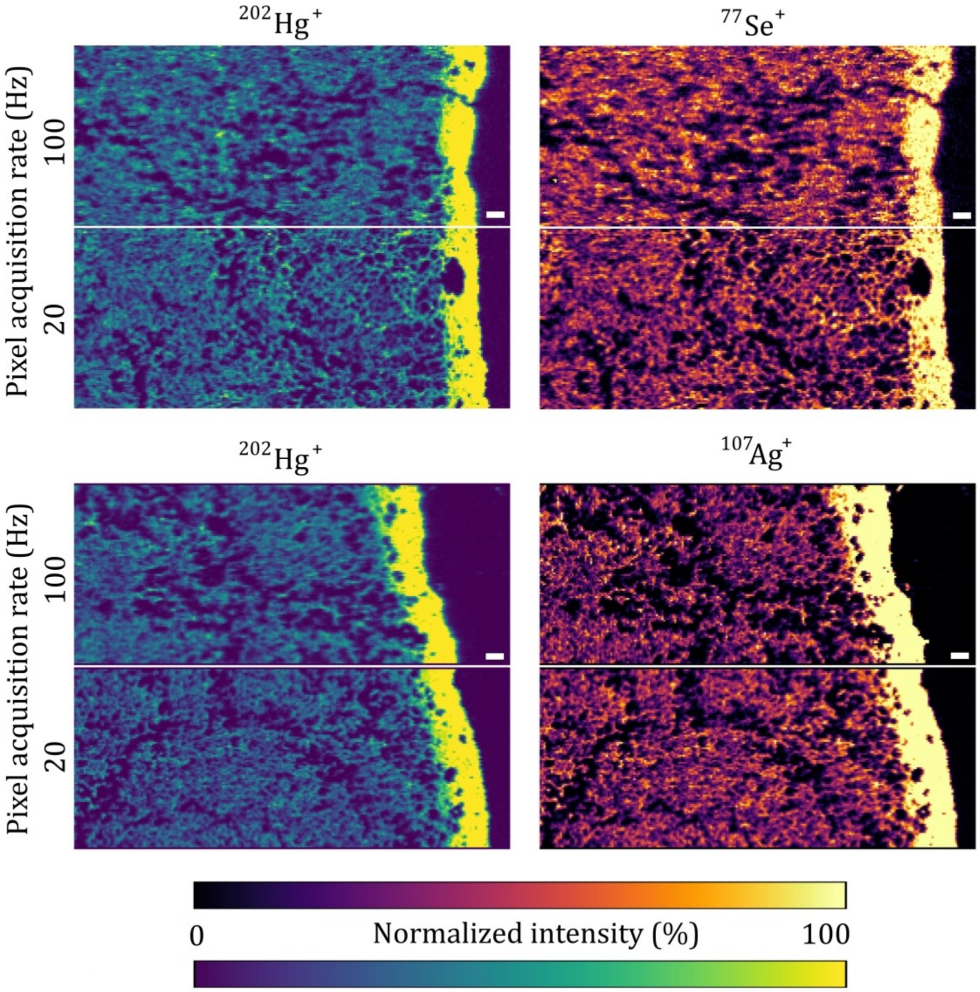

Figure 3

139x149mm (600 x 600 DPI)